Int. J. Radiation Oncology Biol. Phys., Vol. 35, No. 3, pp. 565–577, 1996

0360-3016/96 $15.00 + .00

ELSEVIER

PII: S0360-3016(96)00104-6

● *Technical Innovations and Notes*

SHAPE RECOVERY AND VOLUME CALCULATION FROM BIPLANE ANGIOGRAPHY IN THE STEREOTACTIC RADIOSURGICAL TREATMENT OF ARTERIOVENOUS MALFORMATIONS

ROBERTO FORONI, PH.D.,* MASSIMO GEROSA, M.D.,* ALBERTO PASQUALIN, M.D.,* JEFFREY HOCH, PH.D.,† GRAZIA GIRI, PH.D.,* ARMANDO PASOLI, PH.D.,* ANTONIO NICOLATO, M.D.,* ENRICO PIOVAN, M.D.,* PIERGIUSEPPE ZAMPIERI, M.D.* AND STEFANO LONARDI, PH.D.*

*University of Verona, Neurosurgery Department, University Hospital, Verona, Italy; †Department of Electrical, Computer and Biomedical Engineering, Marquette University, Milwaukee, WI

Purpose: A model for calculating the three-dimensional volume of arteriovenous malformations from biplane angiography.
Methods and Material: Three-dimensional (3D) volume reconstruction is easily feasible with axial, coronal, or sagittal computer tomography (CT) and nuclear magnetic resonance (NMR) scans. On the other hand, radiosurgical treatment of arteriovenous malformations (AVM) is exclusively based on two orthogonal stereotactic projections, obtained with angiographic procedures. Most commonly, AVM volumes have been calculated by assimilating the nidus volume to a prolate ellipsoid. We present an algorithm dedicated to 3D structure reconstruction starting from two orthogonal stereotactic projections. This has been achieved using a heuristic approach, which has been widely adopted in the artificial intelligence domain.
Results: Tests on phantom of different complexity have shown excellent results.
Conclusion: The importance of the algorithm is considerable. As a matter of fact: (a) it allows calculations of complex structures far away from regular ellipsoid; (b) it permits shape recovery; (c) it provides AVM visualization on axial planes.

Gamma knife radiosurgery, AVM, Isodose volumes, 3D reconstruction.

INTRODUCTION

Most of today's stereotactic methodologies for the definition of the target area are based on the computerized analysis of nuclear magnetic resonance or axial tomography data. If the target area is an arteriovenous malformation (AVM), the CT or NMR methods prove ambiguous, or rather, are suitable only for the spatial localization of the lesion, but not for its exact delimitation. The portions of an angiomatous nidus with a faint blood flow may, for example, escape detection through both CT (caused by an insufficient attenuation of the radiation beam) and NMR (due to absence of the vacuum void signal phenomenon); furthermore, both CT- and NMR-based methods are subject to "partial volume artefacts." In this case, therefore, it is necessary to use traditional angiography. The rapid biplanar sequence of the angiographs is selective in localizing the lesion and in defining the composite silhouette both temporally and in anteroposterior (AP) and lateral (LL) projection.

However, what the angiographic procedure alone fails to provide is the possibility of calculating the volume of the lesion with certainty; additionally, determining its three-dimensional (3D) shape is also complicated. At the present time, most neurosurgical centers approximate the lesion to a prolate regular ellipsoid whose axes coincide with the three maximum diameters of the lesion; the uncertainty as to the actual 3D shape of the lesion leaves the question of the best radiation treatment open to debate. Identification of the exact shape reconstructed from only two two-dimensional orthogonal projections, therefore, becomes very important not only for radiosurgery, but also for conventional nonstereotactic radiology and radiotherapy.

The present article proposes a solution to the problem of identifying the 3D shape of lesions and calculating their respective volumes through the use of the two angiographic silhouettes and without assuming any prior knowledge of the object. The numerous tests performed on phantoms of different shapes and volumes confirm the validity of this new type of approach.

Reprint requests to: Roberto Foroni, Ph.D., Divisione di Neuroradiologia, Dipartimento Neurochirurgia, Ospedale Borgo Trento, 37126 Verona, Italy.

Accepted for publication 19 February 1996.

METHODS AND MATERIALS

Patients

During the period of February 1993 to March 1994, 31 patients with cerebral arteriovenous malformation (10% of the cases treated) underwent radiosurgical treatment at the Verona University Neurosurgery Department. The stereotactic radiosurgical procedure was performed with 201 isocentric sources of radioactive cobalt whose characteristics and configurations have been sufficiently described in detail elsewhere (22, 23).

The sample was comprised of 16 male patients ages 13 to 59 years, and 15 female patients ages 14 to 69. Further clinical data will be presented in an article still to be published.

For all patients, according to the normal procedures of stereotactic localization of the lesion, a detailed arteriograph and, if necessary, an NMR (18 of 31 patients) were performed after placement of the 'Leksell frame' on the cranium of the patient and its subsequent attachment to the angiographic bed. From the localization films, the target center and the LL and AP magnification factors were obtained.

Phantom

The setup of the 3D reconstruction algorithm, however, was done and validated on a number of phantoms of different complexity and geometry (Table 1). Two traditional AP and LL radiographs (Fig. 1) of these phantoms, randomly located inside the Leksell system, were taken to determine the limits or the contours, as is also done in normal angiographic stereotactic operations. The volume of the phantoms was calculated by immersing them in measuring probes full of water and by measuring the volume of displaced liquid; the measurement was repeated five times for all phantoms.

Methodology of AVM reconstruction

The reconstruction of a three-dimensional object requires a number of operative or structural postulates, which make it possible to convert two-dimensional contour information into three-dimensional structures (17, 18, 24, 38, 40). With these postulates it is possible, as in a later stage, to perform a topological transformation $R^2 \Rightarrow R^3$.

Structural postulates

1. The structure of the vessel that comprises the body of the nidus forms a chaotic agglomerate that is structurally compact and presents no bifurcations; thus, a 3D function that describes the lesion may be expressed by $T(x,y,z) = 1$ if the coordinates belong to the inside of the lesion, or by $T(x,y,z) = 0$ if they do not (10, 11, 26, 43). The images obtained from two-dimensional projections distinguish only the outline silhouette, but may be inconsistent with regards to internal information. Thus, we have to reject toroidal, helical structures, or structures with multiple bifurcations.

Table 1. Phantom test

Shape	Volume (cc) measured	Volume (cc) calculated
Regular	2.0 ± 0.1	1.85 ± 0.15
Irregular	3.2 ± 0.1	3.0 ± 0.2
Regular	7.6 ± 0.3	7.1 ± 0.4
Irregular	4.5 ± 0.1	4.2 ± 0.2
Irregular	3.5 ± 0.1	3.30 ± 0.15
Regular	12.1 ± 0.3	12.2 ± 0.5

2. The borders of the AP and LL silhouette must not define or simultaneously belong to more than one object (16, 28, 29, 35, 37, 42).
3. There exists a preferential axis, parallel to the head-foot line, the Z axis, around which the two AP and LL biplanar projections emulate a 90° rotation by the object. Therefore, if X_{MC}, Y_{MC}, Z_{MC} are the coordinates defining the geometric center of the lesion (commonly called the matrix center) any rotation around this center may be defined according to the usual rotation rules along the Z axis (1, 4, 8, 9, 26, 30).
4. It is always possible to break the structure of an object down to smaller parts whose complete overall shape is a good approximation of the actual volume and shape of the object (2, 15, 20, 36, 41). The cross-sections of the object for adjacent slices may present sometimes remarkable spatial shifts.

Reconstruction of the model

The operative procedures relating to the construction of a 3D object require the following three procedures: (a) contour detection in the biplanar image, (b) construction of a 3D model, (c) calculation of the volume.

Contour detection

The rapid sequence of both angiographs and their respective subtractions allow for the study of the complex dynamics taking place inside the lesion, whose external border or silhouette appears circumscribed as the entire arteriovenous shunt area. This silhouette is then projected on AP and LL grids, whose horizontal lines are equidistant at 1 mm, amplified to the relative magnification factor. The intersection of these contours along the grid creates an equal pair of AP and LL points according to planes parallel and equidistant from the relative reference system of the matrix center and perpendicular to the Z axis. All the pairs of points having the same z value on both sides of the lesion, are acquired manually by means of a digitizer and represent the input data of the 3D reconstruction algorithm. From this initial operation a list of points $P(x_{ki}, z_i)$, $P(y_{ki}, z_i)$; $k = 1,2$ is obtained. Perpendicular to the z axis the intersections of such points at $z = z_I$ define a list of z consecutive equally spaced slices or cross-sections (Fig. 2). Independently of the length and complexity of the silhouette, it, thus, proves possible to divide a contour into

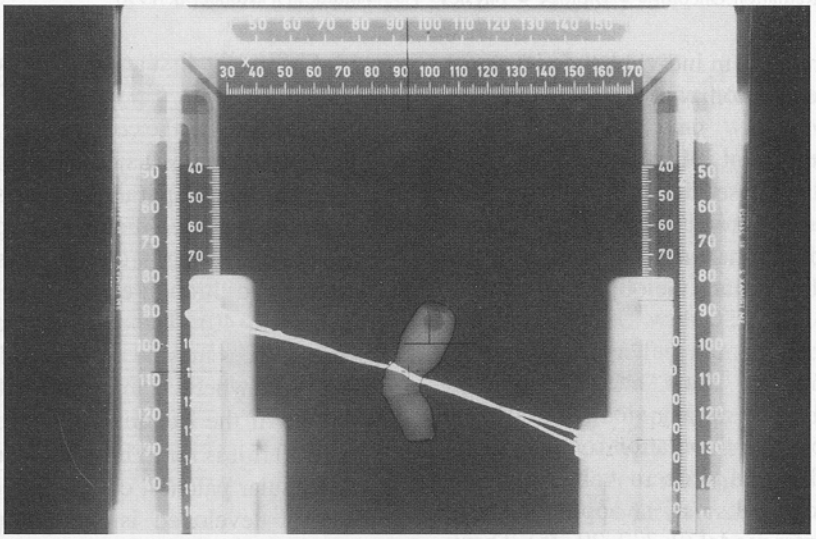

(a)

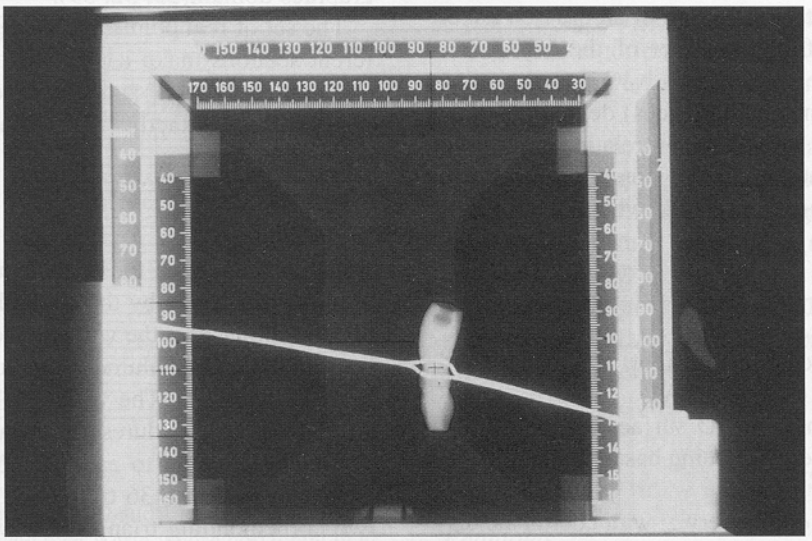

(b)

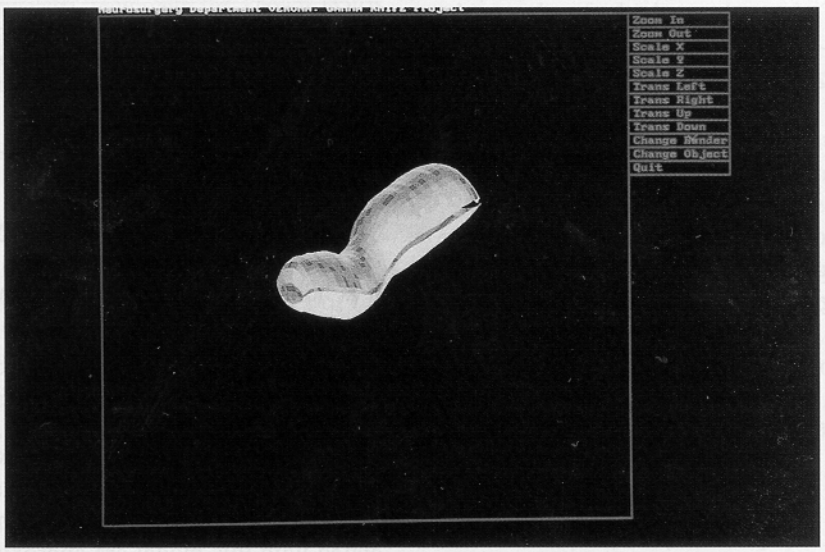

(c)

Fig. 1. From the anteroposterior (a) and lateral (b) orthogonal projections, it is possible to define the form or silhouette of a phantom whose matrix center and relative magnification factors may be calculated. Two ruled series at different enlargements are visible: the smaller scale is nearest to the projection plane; the larger scale is nearest to the projection focus. (c) Represents the reconstructed phantom according to Marching Cubes algorithm.

small sections and examine them individually without error propagation. The acquisition was repeated twice by two different operators.

"If two images from different viewpoints can be placed in correspondence, in the sense that it is known which points in the two images are projected by the same point in space, the intersection of the lines of sight from two matching image points determines the object" (9).

3D reconstruction

A set consisting of at least the four points $P(x_{ki},z_i)$, $P(y_{ki},z_i)$; $k = 1,2$ belonging to the different cross-sections is fitted by an interpolation routine assuming that the any bounded and nonzero values function $\{\phi(x_k, y_k)\}\epsilon z_i$ of each such points may be approximated to piecewise continous elliptic model (2, 3, 7, 29, 35). Therefore, it is possible to obtain a bidimensional contour $U_i\epsilon z_I$ (represented by a concatenation of an ordered list of concentric vertices) defined by a set of the key points $\{(x_k,y_k); k = 1,2\}$. $U_i\epsilon z_I$ (represented by a concatenation of an ordered list of concentric vertices) defined by a set of the key points $\{(x_k,y_k); k = 1,2\}$. In relation to the matrix center for each contour U_i, it is possible to define a preferential point c_i, called centroid, whose 3D coordinates can be defined as:

$$\left(x_{c_i} = \frac{(x_{R_i} + x_{L_i})}{2}; y_{c_i} = \frac{(y_{U_i} + y_{D_i})}{2}; z_{c_i} = z_i\right)$$

where R, L, U, and D denote the right, left, upper, and lower part of the lesion (Appendix A).

In mathematical terms, our 3D surface reconstruction procedure can be considered as being based on the following two steps:

(a) evaluate the centroid c_i for every z_i with coordinate distance $d(c_i)$ from the matrix center or fixed reference frame

$$d(c_i) = \sqrt{\left[\frac{(x_{R_i} + x_{L_i})}{2} - X_{MC}\right]^2 + \left[\frac{(y_{U_i} + y_{D_i})}{2} - Y_{MC}\right]^2 + [z_i - Z_{MC}]^2}$$

(b) reconstruct, from a set of points $\{x_i,y_i \epsilon R^2\}$ and centroids $c_i\epsilon R^3$, a closed polygonal curve whose relative coordinates can be defined as an interpolation of function S satisfying the following conditions:

(i) at every interval $[x_i,x_{i+1}]$, S is a cubic polygonal denoted as

$$S_i = a_i(x - x_i)^3 + b_i(x - x_i)^2 + c_i(x - x_i) + d_i$$

for $i = 0,1,...n(n =$ number of points).

(ii) at each point x_i for $\{i = 0, n\}$ $S(x_i = y_i)$ satisfies $S_{i-1}(x_i) = S_i(x_i)$

$$S'_{i-1}(x_i) = S'_i(x_i)$$

$$S''_{i-1}(x_i) = S''(x_i)$$

with S',S'' as the first and second derivative of the function $S(x)$.

This allows for the construction of an object as if it were composed of many disjointed components, but connected through adjoining parallel sections. Such an object can be described by a three-dimensional polyhedral structure that encompasses regions called faces connected to one another, linked through edges, which in turn, are linked by vertices(18, 40). The segmentation of the network into different faces may be represented by a connection matrix $(CM)(N^2)$, where N represents the number of vertices. $CM_{ij} = 1$ if the i vertex is connected to the j vertex and $CM_{ij} = 0$ if it is not. The aggregate ordered chain of faces or triangular patches, completely covers the surface. The software developed is based on the Marching Cubes (MCub) algorithm (Appendix B), extensively used in 3D graphics domain(25, 32, 39).

The set of real points and those interpolated on the different sections make it possible to obtain a solid model. Only on the two AP and LL planes should the projection of the solid exactly match the two original initial silhouettes.

Volume calculation

The nth bases of the polygonal that belong to the ith sections multiplied by the step relative to the subdivision of the contour give the volume. Contrary to the procedure for the AVM, the volume is measured along the axial sections of the lesion. The volume is calculated according to the following procedures: (a) the area encompassed by the n points belonging to each section is divided into n triangles (in our case 36 triangles); (b) the average area of two corresponding triangles on two consecutive sections is calculated to minimize errors in the event of jagged surfaces; this area is multiplied by the distance between the two consecutive sections; (c) it is added for the 36; (d) it is added for all the sections; (e) spherical caps, whose height is half the average distance between two consecutive sections, and whose radius equals the average radius of the contour of the last two sections, are added to the ends of the volume.

This algorithm was tested on known volumes by acquiring, using a digitizer, sections of regular geometric figures (cylinders and spheres); the average errors associated with this model are approximately 3%.

The values of the AVM volumes calculated with the procedure described above were compared with those obtained by approximating the lesion to a prolate ellipsoid, using the formula

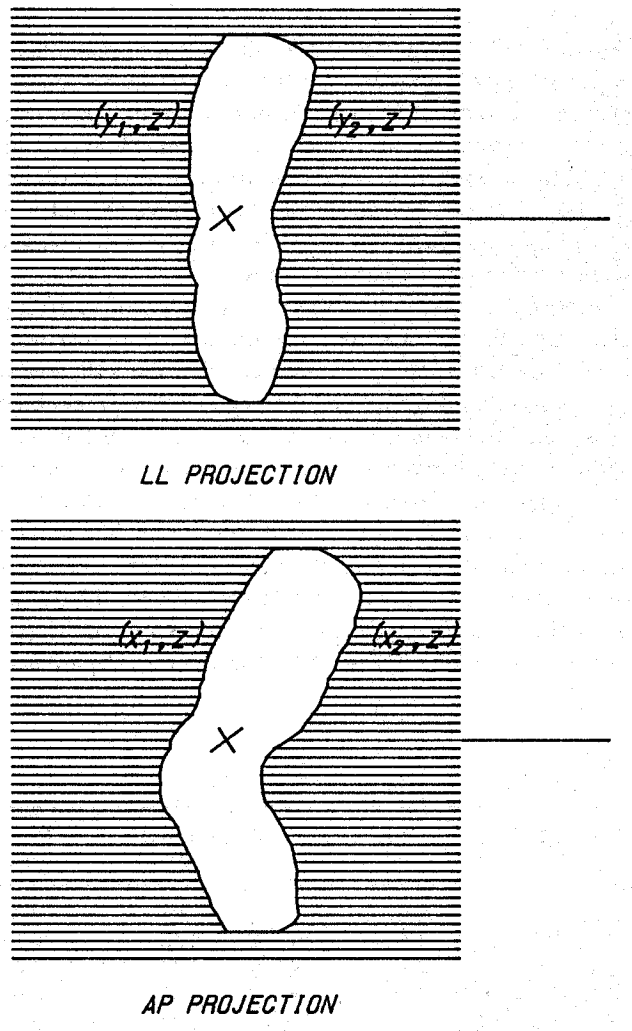

Fig. 2. The figure represents the AP and LL projections of the contours of a phantom placed over a grid whose horizontal lines are 1 mm apart and multiplied by the relative magnification factors. The cross in the center represents the known matrix center. It is, therefore, possible to define the grid contour intersection coordinates. Hence, for each single Z_i there is a series of pairs of points along the XZ_i and XY_i planes.

$$V = \frac{4\pi}{3}abc$$

where a, b, and c denote the three orthogonal axes of the lesion(31).

By means of an isocontour algorithm, the polygonal of the therapeutic isodose was segmented along the z planes from which it was possible to find the corresponding treatment volume.

Computer hardware

All the software used to calculate the isodose relative to the treatment plan was developed on a 3100-30 MicroVax station under VMS Rel. V[1] Operating System and Fortran 77 Compiler. The software for the 3D reconstruction, developed 'in loco' was implemented on a Zenith 486/25 MHz EISA[2] to which two RISC boards were interfaced: the first, a Microway I860/40[3] MHz, based on Intel I860[4] CPU with 32 MBytes RAM running C++ Compiler, for the fast numerical calculations, and the second, a Matrox MG3DU,[5] based on a DSP TMS340C30[6] CPU , for the complex graphic functions. The I860 board creates a 3D structure (triangular or quadrilateral patches) of both the isodose and the lesion; this structure is entered on the Matrox board for display of all the graphic operations on the monitor or alternatively on a plotter (Hewlett Packard HP7550 Plus[7]). In the event of output on the plotter, the program generates a solid 3D figure through a hidden line algorithm developed in cooperation with the Marquette University Department of Computer Science (17, 19).

Calculation times are considerably reduced: less than 3 min for output on the plotter, while the Matrox board gives real time performance for all graphic operations, even complex ones such as volume rendering, hidden lines, zooming, and 3D rotations.

The acquisition of the lesion silhouettes took place with a Calcomp Digitizer,[8] whose maximum margin of error is 1 mm on the average.

RESULTS

Phantoms

Tests conducted on phantoms of different complexity, the results of which are shown in Table 1, clearly confirm the reliability and strength of the algorithm (Table 1). In this table the geometric specifications of six different phantoms and their volumes are indicated; in column 1 a 3D concave structure is indicated as regular, whereas any convex structure is considered irregular. In column 2 the real volumes of the different phantoms are given; the volumes were obtained by immersing the phantoms in water probes and by evaluating the equivalent amount of water displaced. In column 3, the volumes calculated with our algorithm are reported: the agreement between the data in the two columns is extremely satisfactory. The difference between the real and the calculated volume, in fact, is less than 1% in the best instance and 8% in the worst.

[1]Micro Vax and VMS are trademarks of Digital Equipment Corporation.
[2]Zenith 486/25 is a trademark of Zenith Data System.
[3]Number Smasher 860 is a trademark of Microway Inc.
[4]Intel 1860 is a trademark of Intel Corporation.
[5]Matrox MG3DU is a trademark of Matrox Electronic System Ltd.
[6]TMS34030 is a trademark of Texas Instruments Corporation.
[7]HP7550 is a trademark of Hewlett Packard Corporation.
[8]Calcomp Digitizer is a trademark of Calcomp Ltd.

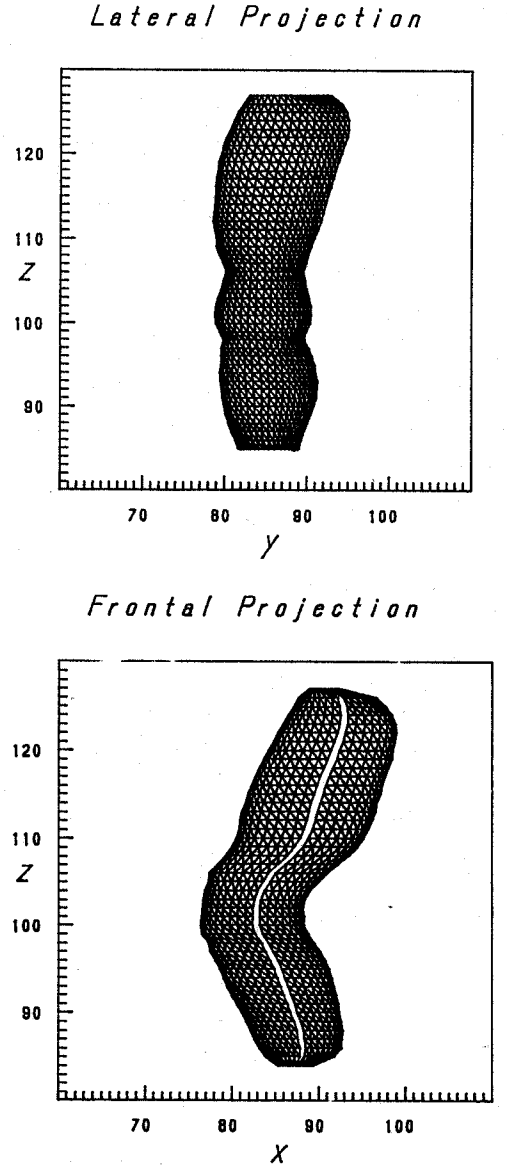

Fig. 3. The 3D reconstruction of the phantom reproduces, in the *XZ* and *YZ* projections, a solid whose external contours give the original silhouette. In the frontal projection for which the patch was not intentionally closed, it is possible to see clearly how the algorithm gives a faithful reconstruction through the decomposition of the object in sufficiently small sections (1 mm) and in the evaluation of the *i*th centroid in relation to the lesion center.

The matching of the reconstructed and reprojected solids, according to their respective magnification factor, on the two orthogonal silhouettes is precise (Fig. 2). Additionally, the forms reproduced by the reconstruction algorithm faithfully reproduce original, real objects, even though such objects had been chosen for their complexity (Fig. 3).

The calculation of error propagation is still under study.

Patients

In Table 2 we reported the results of the 31 patients on whom a volume study was performed. For the 31 patients examined and treated with radiosurgery in our department, we give the volume calculated with our algorithm (column 1) and the one obtained with the ellipsoidal model (column 2). The discrepancies are great, this is obvious, but it is worth noting the fact that of 31 lesions examined only 7 were referable to regular ellipsoids.

In this instance, due to the impossibility of verifying the true volumes, we compare the data obtained with our algorithm to those obtained with the ellipsoidal model, as well as the related discrepancies in percentage terms. In Table 2 we also show the volumes of the therapeutic isodose relevant to the treatment and obtained according to the procedure furnished by the Elekta.[9] On average, the data obtained with the ellipsoidal model are comparable to those obtained with the new algorithm, with a discrepancy less than 10% for 15 out of 31 patients, between 10 and 20% for 8 out of 31 patients, and between 20 and 40% for 8 out of 31 patients.

Table 2. AVM volume

No.	3D Reconstruction (cc)	Ellipsoid (cc)	Error (%)
1	0.94	1.01	7.4
2	4.66	5.60	20.1
3	0.38	0.37	2.6
4	15.40	14.38	6.6
5	2.43	2.77	13.9
6	0.76	0.97	27.6
7	1.07	1.22	14.0
8	2.20	2.14	2.7
9	1.21	1.44	19.0
10	1.02	1.14	11.0
11	1.91	2.27	29.0
12	0.34	0.41	20.0
13	1.12	1.22	8.9
14	2.45	2.34	4.4
15	3.00	3.70	23.0
16	0.29	0.32	13.0
17	0.64	0.61	4.6
18	1.02	0.97	4.9
19	1.93	2.11	9.3
20	0.21	0.29	38.0
21	2.55	2.03	20.4
22	0.15	0.23	53.3
23	0.77	0.77	0.0
24	2.64	2.79	5.7
25	21.38	27.75	29.7
26	8.94	10.45	16.8
27	0.89	0.91	2.2
28	1.50	1.53	2.0
29	1.13	1.23	8.84
30	1.42	1.46	2.8
31	3.64	4.13	13.5

[9] Elekta Instruments Inc.

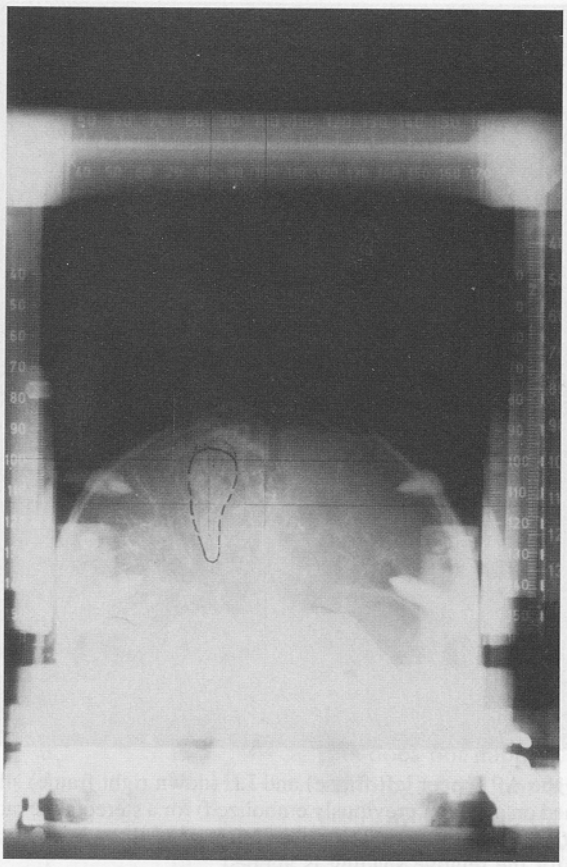

(a)

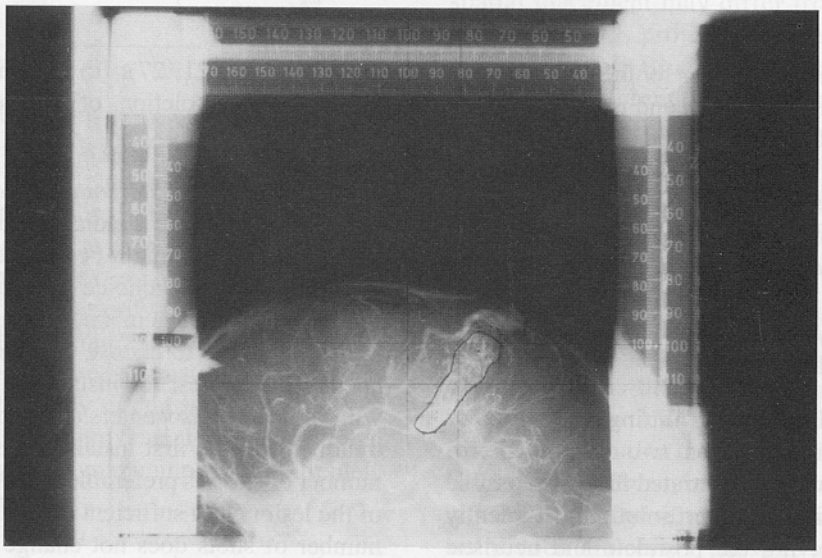

(b)

Fig. 4. Photograph of two radiographic films representing the AP (a) and LL (b) projections of the lesion. The image of the angiographic nidus is highlighted by the blue line drawn by the neuroradiologist.

There is a substantial discrepancy between the volume of the therapeutic isodoses and the volume of the lesion. The volume values of the therapeutic isodoses exceed, on the average, the calculated AVM volumes; in some cases the difference is considerable. This, we believe, is due to lack of knowledge of the 3D shape of the lesion, which results in superfluous irradiation of healthy tissue and an imprecise calculation of the risk factor (see below for details).

The matching of the reconstructed and projected AVM lesions in AP and LL on the two respective silhouettes is exact (Figs. 4 and 5), though most of the forms do not have a regular geometric shape.

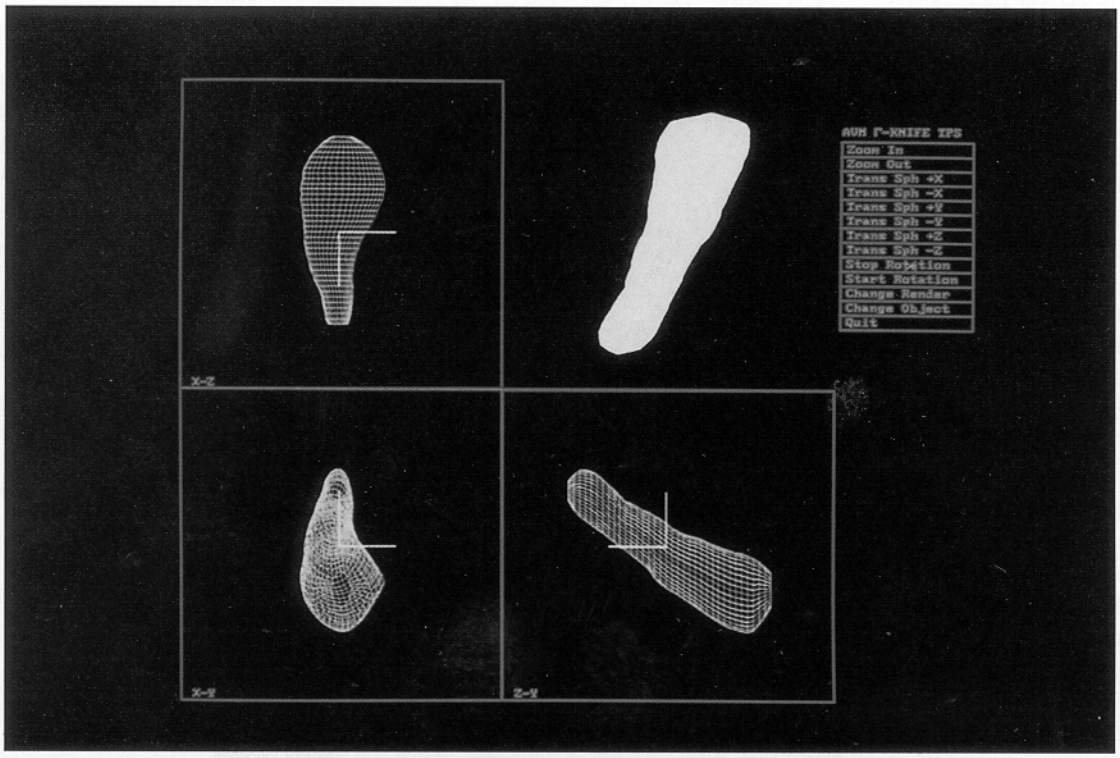

Fig. 5. The figure reproduces the AP (upper left frame) and LL (down right frame) silhouette of an AVM obtained with an angiography (performed on a patient previously embolized) for a stereotactic radiosurgery treatment, whereas the XY reconstruction is on the down left part. The upper left part of the window frame represents the 3D lesion on which Phong's algorithm for the relative shading is applied.

In Table 3 we show the dose values for the treatment performed on the 31 patients (maximum and target dose). The table shows the treatment modalities for the 31 patients studied. In columns 2 and 3 the maximum doses (Gy) and the periphery doses (Gy), respectively, are reported. In column 4, the number of isocenters for each single treatment; in column 5, the types of collimators used.

DISCUSSION

Although a general algorithm permitting recognition of the form of 3D objects starting from two orthogonal projections does not exist, we demonstrated that it is possible to approximate a configuration or solution sufficiently close to reality by applying the postulate and heuristic procedures already being used in the field of stereo vision or in the recognition of shapes from moving scenes.

The calculation of the volume and the reconstruction of a 3D model have distinct advantages, three of which warrant thorough analysis. These are: (a) optimization of the stereotactic treatment through a transformation of the AP and LL projections to axial planes; (b) calculation of the volume and shape of the lesion that must be included in the risk factor formula, relating to the probability of radiation brain complications as predicted according to integrated logistic formula (exponential or quadratic model)(12–14, 21, 27); (c) optimization of the neuroradiologic reconstruction of the lesion in terms of its silhouette.

Optimization of the stereotactic treatment

The data in Table 2 indicate a dose over the periphery much greater than might be expected *a priori*. This is not due to an erroneous choice of treatment, which would be immediately obvious in a normal axial treatment plan, but rather to having to choose between two competing therapeutic modalities, for instance, a stereotactic procedure with one or two isocenters as opposed to a more complex treatment. In the first instance, the choice of a minimum number of shots is preferable if these can cover the borders of the lesion with sufficient certainty. However, a reduced number of shots does not change the distribution of the ellipsoidal dose especially created by the collimators; further, unfortunately, the shape of the lesion, though ellipsoidal (7 out of 31), presents a tilting or bending, which is hard to match to an optimal configuration of the isodoses. Consequently, in at least one of the two projections there is a volume deficiency. The alternative, which requires the use of many shots, improves the matching between the silhouette and the isodose, but its interpretation is difficult in the evaluation of the actual covering of the lesion outside the defined plane in the matrix center coordinates(13, 14, 32, 34, 42). Our algorithm, on the con-

Table 3. Radiation dose (Gy)

No.	Maximum (Gy)	Periphery (Gy)	No. of isocenters	Size of collimators
1	32.0	25.6	1	14
2	48.0	24.0	2	18
3	42.0	25.0	3	8, 4
4	40.0	18.0	3	18
5	40.0	20.0	2	14
6	42.0	25.0	2	14
7	62.5	25.0	4	8, 4
8	31.0	25.0	1	18
9	31.0	25.0	1	18
10	45.0	25.0	2	14, 8
11	31.3	25.0	1	18
12	30.0	15.0	1	14
13	31.3	25.0	1	18
14	35.7	24.0	1	18
15	50.0	25.0	3	18, 14
16	29.0	25.0	1	14
17	40.0	28.0	1	14
18	40.0	20.0	1	14
19	50.0	25.0	3	14, 8
20	50.0	25.0	1	8
21	50.0	25.0	6	8, 4
22	55.0	25.0	2	8, 4
23	27.5	25.0	1	18
24	33.5	20.0	3	18
25	50.0	15.0	4	18, 14
26	50.0	20.0	3	18
27	31.3	25.0	1	18
28	34.0	25.5	1	18
29	50.0	25.0	2	14
30	33.3	25.0	1	14
31	50.0	22.5	4	14, 8

trary, through a transformation from planes XZ and YZ into plane XY (Fig. 6) makes it possible to outline a treatment plan along axial planes, just as it controls the development of the isodoses along these planes; it is only along these axial planes that it is possible to verify the mismatching (over or under dosage) between the isodoses and the silhouettes. This superiority can also be utilized in conventional radiotherapy: an exact calculation of lesion volume allows for a better evaluation of the therapeutic isodose that effectively circumscribes the lesion; the advantage of a 5–10% improvement of the isodose at the periphery is, in terms of maximum dose, extremely relevant to a radiotherapist.

Inclusion of the lesion volume in the risk factor formula

"One difficulty in predicting complication probabilities is the exclusion of the tumor volume in calculating the probability of complications. It seems important to exclude tumor volume since that volume should not contribute to the probability of complications"(12).

As far as we know to date, the 'real' volume of the AVM lesion has not been included in the risk factor calculation. The volume has been considered only in approximate terms, that is, as a fictitious volume of about 2 cc, corresponding to an isodose of 70% of a 14 mm collimator (one of the four required for the gamma unit) in a single-shot treatment or in the case of a higher isodose covering the entire lesion in multiple-shots treatment. In the latter case, however, how is it possible to evaluate the highest isodose that includes the lesion(13, 14)? If, for instance, the evaluation is done on the matching isodose silhouettes a conceptual error of calculation with devastating consequences is introduced.

"The best method of doing this would be with a computer program which produces a 3D reconstruction of the tumor volume and subtracts this from any dose-volume histogram"(12). In fact, our reconstruction algorithm does precisely this.

Optimization of neuroradiological procedures for AVM definition

Our algorithm is fundamentally based on the assumption that the lesion seen in the two AP and LL projections has the same length in relation to the Z axis, or, in other words, that the lesion is equal to the perpendicular projection of the same object. This is likely for all 31 cases of AVM treated in our department, in addition, obviously, to all the phantoms we analyzed. If this does not happen, there are two possibilities: (a) the radiologist did not obtain an exact definition of the lesion; in this case the control in z is useful to redefine the alignment conditions and the setup of the angiographic machine, of the angiographic bed(5, 6). (b) A spatial placement may differ from the silhouette in the two AP and LL projections; this could be the result of a double supply (that is a double dynamics) of contrast medium at different times for the respective projections. In this case, unfortunately, no solution can be found, and the algorithm for the calculation of the volume can be applied only on z of equal value. In this particular case, the integration of angiographic data with CT or NMR information may prove to be vital(33).

CONCLUSION

How valid is the proposed model for the 3D reconstruction of the AVM shape? As of yet, no speculative research or solution for this vitally important subject has been proposed in stereotactic neurosurgery studies. Reconstruction algorithms are obviously not able to rebuild each and every possible object. As proposed in this article, exact reconstruction means rebuilding an object with an arbitrarily 'high precision' by reproducing its silhouette as observed through predefined points of view.

Therefore, this first solution we present may provide the basis for further and more detailed research, which should include densitometer analyses and interfaces done in real time with the data from sections obtained from nuclear resonance or computer tomography. We believe that the exact perimeter and the exact shape of an AVM can be determined only through a multimodal approach,

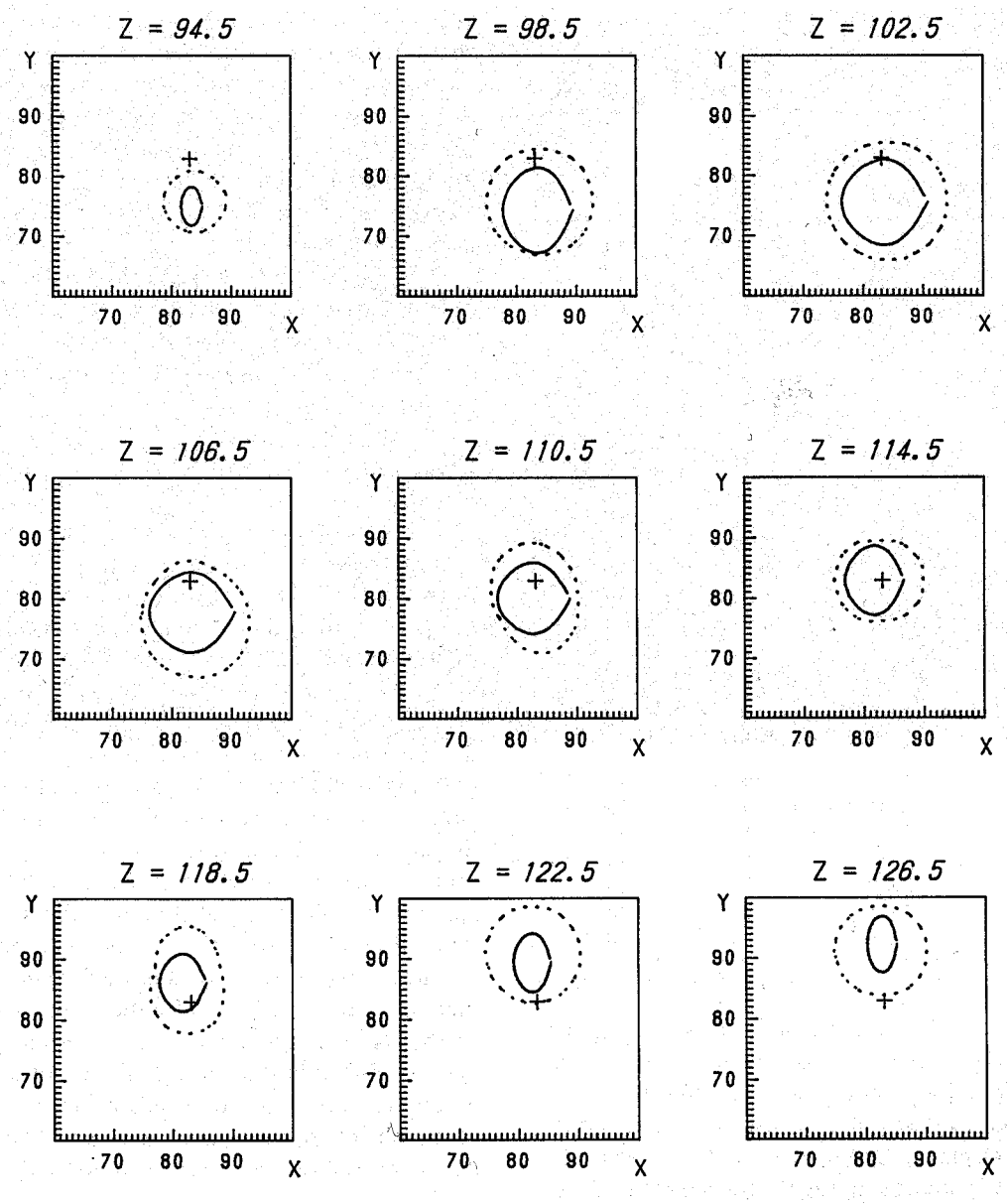

Fig. 6. Axial projections of 3D isodoses (dotted line) superimposed on the lesion contour (solid line) of the AVM presented in Fig. 5. The cross inside the square represents the lesion matrix center, whose coordinates are x_{mc}, y_{mc}, and z_{mc}. The algorithm is particularly useful because it makes it possible to verify the matching isodose-contours on planes different from those in *XZ* and *YZ*.

thus bypassing the misrepresentation that may ensue from exclusively angiographic or from exclusively CT or NMR data (33). Further, the mathematical-graphic procedures used are general and may be extended with sufficient reliability to the fields of neuroradiology or conventional brachytherapy.

REFERENCES

1. Aloimonos, J. Computing shape from shading and motion. Int. Conf. Art. Intel. 2:738–741; 1987, Milano.
2. Asada, M. Determining cylindrical shape from contour and shading. Int. Conf. Art. Intel. 2:797–800; 1987, Milano.
3. Ballard, D. Generalizing the hough trasform to detect arbitrary shapes. Pattern Recognit. 13:111–122; 1981.
4. Blake, A.; Zisserman, A. Visual reconstruction artificial intelligence. Cambridge, MA: MIT Press; 1987.
5. Bova, F. J.; Friedman, W. A. Stereotactic angiography: An inadequate database for radiosurgery? Int. J. Radiat. Oncol. Biol. Phys. 20:891–895; 1991.
6. Brummer, M.; Mersereau, R.; Eisner, R.; Levine, R. Automatic detection of brain contours in MRI data sets. IEEE Trans. Med. Imaging 12:153–166; 1993.
7. Chang, S. K.; Chow, C. K. The reconstruction of three dimensional objects from two orthogonal projections and

its application to cardiac cineangiography. IEEE Trans. Comp. C-22:18–28; 1973.
8. Chang, S. K.; Wang, Y. R. Three dimensional object reconstruction from orthogonal projections. Patt. Recognit. 7:167–176; 1975.
9. Chung, C. R. Deriving 3D shape descriptors from stereo using hierarchical features. PhD Dissertation. Univ. Southern Calif.; 1992.
10. Close, R. Automatic 3D recostruction of vascular geometry from two orthogonal angiographic image sequences. UCLA PACS Research, Medical Imaging Division; 1991.
11. Fisher, R. Model Invocation for three dimensional scene understanding. Int. Conf. Art. Intel. 2:805–807; 1987.
12. Flickinger, J. An integrated logistic formula for predictions of complications from radiosurgery. Int. J. Radic. Oncol. Biol. Phys. 17:879–885; 1990.
13. Flickinger, J.; Lunsford, L.; Kondziolka, D. Assessment of integrated logistic tolerance predictions for radiosurgery with the gamma knife. In: Steiner, L., ed. Radiosurgery: Baseline and trends. New York: Raven Press; 1992.
14. Flickinger, J.; Steiner, L. Radiosurgery and the double logistic product formula. Radiother. Oncol. 17:229–237; 1990.
15. Fright, R.; Linney, A. Registration of 3D head surfaces using multiple landmarks. IEEE Trans. Med. Imaging 12:515–520; 1993.
16. Hebert, M.; Kanade, T. The 3D profile method for object recognition. Proceedings of the Conference on Comp. Vision and Pattern Recognition San Francisco; 1985.
17. Hedgley, D. A general solution to the hidden line problem. NASA software documentation, ARC-11446; 1982.
18. Higgins, W. E.; Morice, C.; Ritman, L. Shape based interpolation of tree-like structures in three dimensional images. IEEE Trans. Med. Imaging 12:439–450; 1993.
19. Hsu, W. I.; Hock, J. L. An algorithm for the general solution of hidden line removal for intersecting solids. Comput. Graphics Appl. 17:67–87; 1991.
20. Kitamura, K.; Tobis, J.; Sklansky, J. Estimating the 3D skeletons and transverse areas of coronary arteries from biplane angiograms. IEEE Trans. Med. Imaging 7:173–187; 1988.
21. Larson, B.; Liden, K.; Sarby, B. Irradiation of small structures through the intact skull. Acta Radiol. Oncol. Radiat. Phys. Biol. 13:512–534; 1974.
22. Leksell, L. The stereotactic method and radiosurgery of the brain. Acta Chir. Scand. 102:316–319; 1951.
23. Leksell, L. Cerebral radiosurgery. Acta Chir. Scand. 134:585–595; 1968.
24. Longuet-Higgins, H. A computer algorithm for reconstructing a scene from two projections. Nature 293:133–135; 1981.
25. Lorensen, W.; Cline, H. Marching cubes. A high resolution 3D surfaces construction algorithm. Comput. Graphics 21:163–169; 1987.
26. Malik, J. Recovering three dimensional shape from a single image of curved objects. Int. Conf. Art. Intel. 2:734–737; 1987.
27. Marks, M. P.; Delapaz, R. L.; Fabrikant, J. I.; Frankel, K. A.; Phillips, M. H.; Levy, R. P.; Enzmann, D. R. Intracranial vascular malformations: Imaging of charged-particle radiosurgery. Part II. Complications.. Radiology 168:457–462; 1988.
28. Mohan, R.; Nevatia, R. Using perceptual organization to extract 3D structures. IEEE Trans. Pattern Anal. Machine Intel. 11:1121–1139; 1989.
29. Moreton, H.; Sequin, C. Functional optimization for fair surface design. Comput. Graphics. 26:167–176; 1992.
30. Nguyen, V. Exploiting 2D topology in labeling polyhedral images. Int. Conf. Art. Intel. 27:787–789; 1987.
31. Pasqualin, A.; Barone, G.; Cioffi, F.; Rosta, L.; Scienza, R.; Da Pian, R. The relevance of anatomical and hemodynamic factors to a classification of cerebral arterio-venous malformations. Neurosurgery 28:370–379; 1992.
32. Robb, R.; Barillot, C. Interactive display and analysis of 3D medical images. IEEE Trans. Med. Imag. 8:217–225; 1989.
33. Spiegelman, R.; Friedman, W. A.; Bova, F. J. Limitations of Angiographic target localization in planning radiosurgical treatment. Neurosurgery 30(4):619–624; 1992.
34. Steiner, L.; Lindquist, C.; Steiner, L. Radiosurgery. In: Symon, L., ed. Advances and technical standards in neurosurgery. New York: Springer Verlag; 19:19–95, 1992.
35. Stevens, K. The visual interpretation of surfaces contours. Artif. Intellig. 17:47–73; 1981.
36. Sun, Y. Automated Identification of vessel contours in coronary arteriograms by an adaptive tracking algorithm. IEEE Trans. Med. Imag. 8:78–87; 1989.
37. Tran, L. V.; Bahn, R. C.; Sklansky, J. Reconstructing the cross sections of coronary arteries from biplane angiograms. IEEE Trans. Med. Imag. 11:517–529; 1992.
38. Tsai, R. Multiframe image point matching and 3D surface reconstruction. IEEE Trans. Pattern Anal. Machine Intellig. 5:159–173; 1982.
39. Turk, G. Retiling polygonal surfaces. Comput. Graphics 26:55–64; 1992.
40. Ulupinar, F.; Nevatia, R. Shape from contours: SHGCs. In: Proc. IEEE Int. Conf. Computer Vision 582; 1990.
41. Ulupinar, F.; Nevatia, R. Inferring shape from contours for curved surfaces. Atlantic City: Proceeding International Conference Pattern Recognition. 1990:147–154.
42. Xia, W.; Lu, W. Correspondence analysis for regional tracking in coronary arteriograms. IEEE Trans. Med. Imag. 11:153–160; 1992.
43. Xu, G.; Tsuji, S. Recovering surface shape from boundary. Int. Conf. Art. Intel. 2:731–733; 1987.

Appendix A

```
read_data_file:        input : data from Digitizer; file_format: float x, z_ap , float y, z_ll
                       output : five float arrays: x_left, x_right, , y_up, y_down, , z3d; length_of_array= length_of_avm
void read_the_data_file() {
FILE *stream; char *string;
stream = fopen(string, 'r');
for (i=0; i < lenght_of_avm; i++)          fscanf(stream, "%f %f %f", &x_right[i], &x_left[i], &z_ap[i]);
for (i=0; i < lenght_of_avm; i++)          fscanf(stream, "%f %f %f", &y_up[i], &y_down[i], &z_ll[i]);
fclose(stream);
fflush(stream);
for (i=0; i < lenght_of_avm; i++)          z3d[i] = (z_ap[i] + zll[i]) / 2.;
for (i=0; i < lenght_of_avm; i++) {
        x_mat[i][0] = x _right[i];     x_mat[i][2] = x_left[i];     x_mat[i][1] = x_mat[i][3] = 0.;
        y_mat[i][1] = y _up[i];        y_mat[i][3] = - y_down[i];   y_mat[i][0] = y_mat[i][2] = 0.;
        }
return; }

construct_a_vertex_chain   input : five float arrays: x, y, true_z; lenght_of_array= lenght_of_avm
                           output : ordered stack of 36 3D vertex array x3D, y3D, z3D anticlockwise
void construct_a_vertex_chain() {
for (i=0; i < lenght_of_avm; i++) {
        for (temp=0; temp < 4; temp++) {
                x_temp[temp] = x_mat[i][temp];
                y_temp[temp] = y_mat[i][temp];
                }
        x_centroid_zi = (x_temp[0]+x_temp[2])/2.;
        y_centroid_zi = (y_temp[1]+y_temp[3])/2.;
        for (temp=0; temp < 4; temp++) {
                if (x_temp[temp] != 0.)  x_temp[temp] = x_temp[temp]- x_centroid_zi;
                if(y_temp[temp] != 0.)   y_temp[temp] = y_temp[temp] - y_centroid_zi;
                }
        interpolate (x_temp, y_temp, x3d_interp, y3d_interp);
        }
}
```

Appendix B

```
/*
```

The Marching Cube algorithm, among the numerous procedures that allow three dimensional graphic visualization, belong to those defined as 'object space' oriented, meaning that it can display 3D multiple surfaces through stacks of constant density contours. The contours are defined through a finite set of 3D vertices and the surfaces (triangular patches) through adjacent vertices with the normals at the vertices. The advantage of that procedure is concerning the capability of derive inter-slice connectivity, and surface gradient.

```
*/
reduced_marching_cube   input:  float array of stak of contours defined by x3d_interp, y3d_interp, z3d vertex anticlockwise
                        output:  tile _of_3d_triangular patches with 3d_vertex_normal for Gourand shading
void reduce_marching_cubes(x3d_interp, y3d_interp, z3d) {
FILE *matrox;
matrox = fopen("TILE", 'w');
 for (i=0; i< lenght_of_avm -1; i++) {
        for (j=0; j< n_sections_zi; j++) {
                /*cross product of two consecutive vertex using right hand rule*/
                ax= x3d_interp[i+1][j] - x3d_interp[i][j];
                ay= y3d_interp[i+1][j] - y3d_interp[i][j];
                az= z3d[i+1][j] - z3d[i][j];
                bx= x3d_interp[i][j+1] - x3d_interp[i][j];
                by= y3d_interp[i][j+1] - y3d_interp[i][j];
                bz= z3d[i][j+1] - z3d[i][j];
                x3d_normal= (ay * bz) - (az * by);
                y3d_normal= (ax * bz) - (az * bx);
                z3d_normal= (ax * by) - (ay * bx);
                /*normals must be normalized*/
                normalization= sqrt(pow(x3d_normal, 2.) + pow(y3d_normal, 2.) + pow(z3d_normal, 2.));
                x3d_n[j] = x3d_normal/normalization;
                y3d_n[j] = y3d_normal/normalization;
                z3d_n[j] = z3d_normal/normalization;
                fprintf(matrox, "%f %f %f\n", x3d_n[j], y3d_n[j], z3d_n[j]);
                fprintf(matrox, "%f %f %f\n", x3d[i][j], y3d[i][j], z3d[i][j]);
                }
        }
}
```

The total source listing is very long. We produced a partial listing, but the complete source C Code is available upon request.